ACS Partner Journal

CHEMICAL & BIOMEDICAL IMAGING

pubs.acs.org/ChemBioImaging

Letter

Supertemporal Resolution Imaging of Membrane Potential via Stroboscopic Microscopy

Luxin Peng and Peng Zou*

Cite This: *Chem. Biomed. Imaging* 2023, 1, 448−460

Read Online

ACCESS | Metrics & More | Article Recommendations | Supporting Information

ABSTRACT: Membrane potential and its fluctuation are fundamental biophysical phenomena essential to cellular activities and functions. Compared to traditional electrode-based techniques, the optical recording via developed genetically encoded voltage indicators (GEVIs) offers a combination of noninvasiveness, high spatial resolution, and increased measurement throughput. However, its application is limited by the insufficient acquisition rate and time accuracy of the camera. Here we design and apply a stroboscopic illumination scheme to boost the temporal resolution of voltage imaging, while simultaneously eliminating the artifacts caused by nonsynchronized exposure in the rolling-shutter mode. We demonstrate that commonly used GEVIs are compatible with stroboscopic voltage imaging (SVI), and our SVI scheme offers a 5-fold faster acquisition frame rate than that of conventional continuous illumination. The GEVIs tested maintain high sensitivities in the SVI mode, supporting faithful reports of intracellular depolarization waveform and intercellular gap junction-mediated depolarization coupling in human embryonic kidney 293T (HEK 293T) cell populations. SVI allows resolving the action potential (AP) waveform with less distortion and mapping action potential initiation and propagation dynamics in cultured neurons in kilohertz, beyond the restriction from the camera in the field of view.

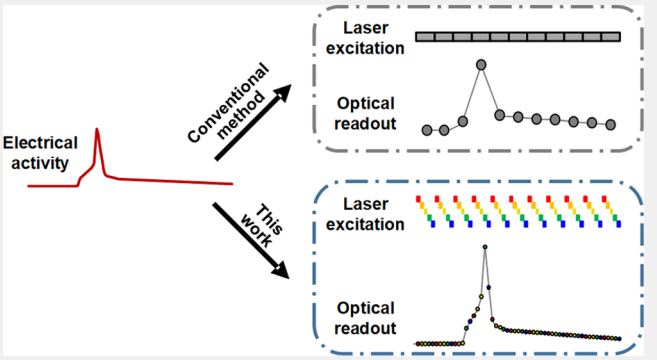

KEYWORDS: *Voltage imaging, Supertemporal resolution, Stroboscopic imaging, Genetically encoded voltage indicators, Action potential propagation*

INTRODUCTION

Bioelectricity is a fundamental biophysical phenomenon that is essential to neural activities. In the nervous system, electrical information is integrated at the soma to trigger the firing of action potentials (APs), which propagate through the neurites to distal ends of the axon and initiate the release of neurotransmitters to stimulate neighboring neurons through the synaptic clefts. Our understanding of the detailed mechanism of the integration, initiation, and propagation of APs depends critically on our ability to map neuronal membrane potentials with millisecond temporal resolution and submicrometer spatial resolution.

Over the past decade, several voltage-sensitive fluorescent probes have been developed to optically record membrane potential dynamics. Among these, genetically encoded voltage indicators (GEVIs) have been applied to report AP and subthreshold membrane potential fluctuations in cell cultures,[1] brain slices,[2] and living animals.[3−5] Compared to traditional electrode-based techniques such as whole-cell patch clamp and high-density multielectrode arrays (HD-MEA), the optical recording of AP offers a combination of noninvasiveness, high spatial resolution, and increased measurement throughput.[6,7] For example, ASAP3 and QuasAr2 enable the high-fidelity recording of AP spike frequency *in vivo* and the mapping of the AP initiation and propagation dynamics across neurite structures in cultured hippocampal neurons.[8,9] These improvements have been summarized in several recent reviews.[10−12]

Despite advancements of voltage indicators over the past decade, the optical information provided by GEVIs is often limited by the insufficient acquisition rate and the timing accuracy of the imaging hardware. Owing to their faster readout speed and larger field-of-view (FoV), scientific-grade complementary metal oxide semiconductor (sCMOS) cameras are typically more favored choices over electron-multiplying charge-coupled device (EMCCD) cameras in kilohertz (kHz) voltage imaging applications.[13,14] For all types of detectors, there is a general compromise between acquisition rate and FoV. For example, running the sCMOS cameras at a 1 kHz imaging frame rate would require sacrificing the FoV by 90%,

Received: April 24, 2023
Revised: June 6, 2023
Accepted: June 21, 2023
Published: July 20, 2023

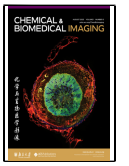

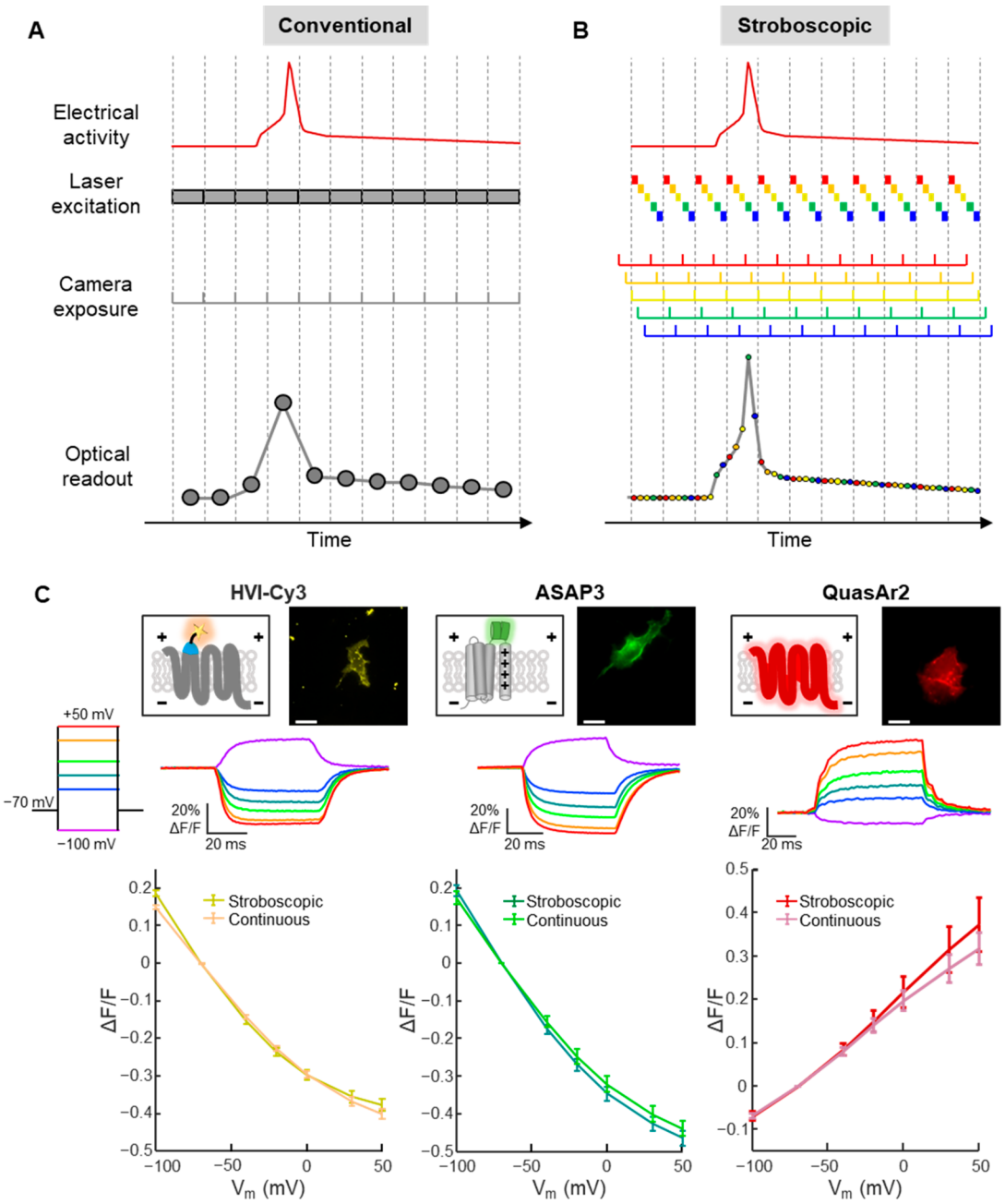

Figure 1. Stroboscopic voltage imaging with genetically encoded indicators. (A,B) Cartoon scheme of the improvement of stroboscopic voltage imaging (SVI) from substituting continuous (A, gray) with stroboscopic illumination (B, rainbow-colored, with a laser duty cycle of 20%). For compensating the bias in the data from one specific strobing position in every horizontal line due to the rolling-shutter readout, the phase of each imaging sequence is shifted by one unit of the duty cycle. (C) Characterization of commonly used GEVIs: HVI-Cy3 (n = 10), ASAP3 (n = 10), and QuasAr2 (n = 6). The voltage sensitivity is measured in the $F-V$ curve for each indicator in either SVI mode (darker trace) or conventional mode (lighter trace). The $F-V$ curves are measured from the steady state fluorescence of GEVIs expressed in HEK 293T cells when the membrane potential is voltage clamped at V_m = −100, −70, −40, −20, 0, 30, and 50 mV. The fluorescence responses are normalized to the baseline fluorescence at V_m = −70 mV. Data were acquired at 1474 and 295 Hz for stroboscopic and conventional voltage imaging, respectively. Scale bar = 20 μm.

which severely limits its capability of mapping AP propagation. This situation is further complicated by the rolling-shutter mode, the fastest readout mode of the sCMOS camera where adjacent rows of the camera chip are exposed and read out sequentially with a delay of approximately 10 μs per row. This unsynchronized recording could distort the recorded AP waveforms.

Herein, we report the design and application of a stroboscopic illumination scheme to boost the temporal resolution of voltage imaging, while simultaneously eliminating the artifacts caused by nonsynchronized exposure in the rolling-shutter mode. Stroboscopic illumination was initially introduced in photography as a means to mitigate motion blur.[15,16] It was later applied to fluorescence microscopy to improve the timing accuracy when tracking rapidly moving biomolecules.[17−21] In stroboscopic imaging, the temporal resolution is determined by the timing and duration of light pulses rather than camera exposure. For example, a lower duty

https://doi.org/10.1021/cbmi.3c00054
Chem. Biomed. Imaging 2023, 1, 448−460

cycle of the light pulse could lead to a higher timing accuracy of image acquisition, given the same camera exposure time. Another advantage of pulsed illumination is the simultaneous acquisition of the entire imaging FoV on the camera chip, which can be used to eliminate the artifacts from unsynchronized exposure when the camera is running in the rolling-shutter mode.

In the current study, we demonstrate that commonly used GEVIs (e.g., ASAP3,[8] QuasAr2,[9] HVIs[1]) are compatible with stroboscopic voltage imaging (SVI). Our SVI scheme offers a 5-fold faster acquisition frame rate than the conventional continuous illumination, while the GEVIs tested maintain their high sensitivities in the SVI mode, enabling faithful report of both intracellular depolarization waveform and intercellular gap junction-mediated depolarization coupling in human embryonic kidney 293T (HEK 293T) cells. We further apply SVI to map the details of action potential initiation and propagation dynamics in cultured rat hippocampal neurons.

RESULTS

Design and Characterization of the SVI Scheme

In conventional voltage imaging with continuous laser excitation, the acquisition frame rate is determined by the exposure time of the camera and is often inversely related to the available FoV on the camera chip (Figure 1A). In the case of sCMOS cameras with a full FoV frame rate of 100 Hz, imaging in the kHz regime would sacrifice 90% of the camera chip. When voltage imaging is performed at a low acquisition rate, the optical readout is low-pass filtered, which severely distorts the action potential waveform (Figure 1A). In the stroboscopic illumination mode, however, the temporal resolution is determined by the duration of strobe light whose duration is several-fold shorter than the camera exposure time, thus increasing the timing accuracy of each sampling (Figure 1B). If the laser exposure is only 20% of the camera exposure, the effective timing acquisition is 5-fold better. However, in this scheme, the duration between two consecutive strobes is still equal to the camera exposure time, which does not improve the actual acquisition rate of voltage imaging.

To achieve a higher acquisition rate, the stroboscopic imaging sequence is repeated five times, each time shifting the phase of the strobe light by 20% of the camera exposure time. When these series of imaging sequences are aligned together, they effectively fill in the gaps of each other. The reconstructed image series thus offers a 5-fold higher acquisition frame rate than the conventional imaging method. In principle, a lower duty cycle of the pulsed laser illumination can lead to better temporal accuracy and a higher acquisition rate of voltage imaging. On the flip side, however, a lower duty cycle requires more repeated acquisitions to cover all the phases, which may introduce additional noise. Given that voltage imaging at 500 Hz is often sufficient to capture the action potential waveform and that the full-frame acquisition rate of the sCMOS camera is 100 Hz, a 5-fold improvement in the temporal resolution would be appropriate. We thus chose 5-phase SVI with a 20% duty cycle of the laser illumination.

Of note, this imaging scheme requires repeated acquisition of the same biological processes at least 5 times to produce the high temporal resolution image series. Since the initiation of action potentials could be reliably triggered and averaged, we reason that the stroboscopic imaging scheme could be applicable for voltage imaging analysis (Figures S1 and S2). However, since conventional voltage imaging has been done only in the continuous imaging mode, it was unclear whether the commonly used voltage indicators would maintain their high voltage sensitivity in the pulse-illuminated SVI mode. Notably, it has been reported that the voltage sensitivity of rhodopsin-based indicators differs considerably when they are under one-photon illumination versus two-photon excitation.[22,23] Thus, it is important to first characterize the sensitivity of voltage indicators experimentally. To compensate for the signal-to-noise ratio (SNR) loss caused by the lower laser duty cycle, we increased the illumination power density in SVI by 5-fold than in conventional imaging. Thus, the total illumination dosage is identical in SVI and the conventional method.

We chose ASAP3, QuasAr2, and HVI-Cy3 as representative voltage indicators for testing their dynamic ranges under stroboscopic illumination in cultured HEK 293T cells. ASAP3 senses the membrane potential (V_m) fluctuations via the voltage-driven conformational changes in the voltage sensing domain (VSD) derived from a *Gallus gallus* voltage-sensing phosphatase.[8] QuasAr2 and HVI-Cy3 feature voltage-sensing rhodopsin scaffolds that report changes in the membrane potential via the electrochromic effect.[1,9] In all cases, the cellular membrane potential was controlled via the whole-cell voltage clamp and varied transiently from −70 to −100, −40, −20, 0, 30, and 50 mV. The fluorescence responses of the selected GEVIs were acquired simultaneously under either stroboscopic or continuous illumination mode, with the identical setting of camera exposure time. The steady-state fluorescence in the step-like fluorescence response at each V_m from the entire clamped cell was normalized to −70 mV and used for characterization (Figure 1C). The same measurement was also performed on another two rhodopsin-based voltage indicators, HVI-AF594 and Ace-D81S-mOrange2 (Figure S3).[24]

The fluorescence response curves of all three candidates in the SVI mode are almost identical to those in the conventional mode. For example, when the V_m was varied between −70 mV and 30 mV, the fluorescence of ASAP3 exhibited a fractional change ($\Delta F/F_0$) of −42.5 ± 1.9% (mean ± SEM) in the SVI mode, while its voltage sensitivity in the conventional imaging mode was measured to be −40.0 ± 2.2%. The same trend was observed in QuasAr2 ($\Delta F/F_0$ = 37.3 ± 6.2% in SVI versus 31.8 ± 3.6% in conventional) and HVI-Cy3 ($\Delta F/F_0$ = −35.4 ± 1.6% in SVI versus −36.8 ± 1.2% in conventional). We even observed a slight increase in the voltage sensitivity of QuasAr2 and ASAP3 in the SVI mode (Figures 1C and S4).

Similarly, when cells were hyperpolarized from −70 to −100 mV, comparable fluorescence responses were observed in the SVI mode versus the conventional mode for ASAP3 ($\Delta F/F_0$ = 19.3 ± 1.5% versus 17.3% ± 1.3%), QuasAr2 ($\Delta F/F_0$ = −6.8 ± 1.0% versus −6.7 ± 0.6%), and HVI-Cy3 ($\Delta F/F_0$ = 18.5 ± 0.8% versus 15.0 ± 0.5%) (Figures 1C and S4). Similar results were observed for HVI-AF594 and Ace-D81S-mOrange2 (Figures S3 and S4). It is worth noting that the signal-to-noise ratios (SNRs) of HVI-Cy3, HVI-AF594, and Ace-D81-mOrange2 drop by more than half when measured under the SVI mode. For ASAP3 and QuasAr2, the SNRs remain similar in the SVI and conventional imaging modes (Figure S5). This indicator-specific decrease in SNR may stem from the unique biophysical properties of eFRET-based GEVIs, such as the photocycles and transient photocurrents. Together, these data

https://doi.org/10.1021/cbmi.3c00054
Chem. Biomed. Imaging 2023, 1, 448−460

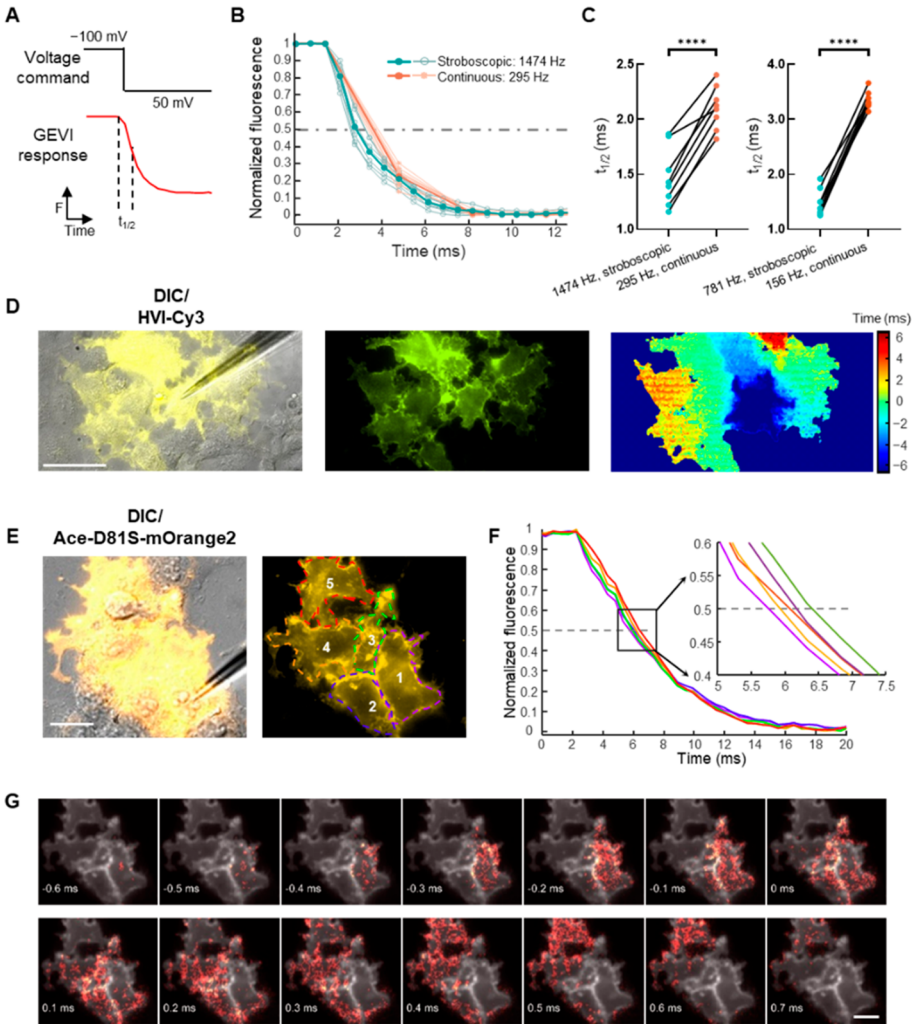

Figure 2. Stroboscopic voltage imaging in electrically coupled mammalian cells. (A) Cartoon depiction of GEVI kinetic definition to a 150 mV V_m depolarization. (B,C) Comparison of the fluorescence decay in HEK 293T cells expressing HVI-Cy3 (n = 8) to a −100 to 50 mV V_m transient recorded between stroboscopic (teal) and continuous illumination (orange) at 1474 and 295 Hz, respectively. Bold lines and solid markers indicate the averaged curves. Dashed lines and hollow markers indicate data from every single cell (B). The measured fluorescence decay half-time ($t_{1/2}$) values are plotted in (C). (D) Brightfield, epifluorescence images, and fitting of the gap junction-mediated long-range depolarization propagation in HEK 293T cells expressing HVI-Cy3 extracted by subframe linear interpolation from SVI data. Scale bar = 50 μm. (E) Brightfield and epifluorescence images of five HEK 293T cells expressing Ace-D81S-mOrange2. Scale bar = 20 μm. (F) Normalized fluorescence decay curves of the five selected cells in (E) to a −100 to 50 mV V_m transient recorded via SVI, with a zoom-in view of the outlined region on the right. SVI Data were acquired at 1958 Hz. (G) Image sequences (Δt = 0.1 ms) from a subframe linear interpolated movie generated from the timing delay in gap junction-mediated depolarization calculated for the field of view in (E). Scale bar = 20 μm.

demonstrate that stroboscopic illumination is compatible with commonly used voltage indicators.

Mapping gap Junction-Mediated Electrical Coupling with SVI

To demonstrate the better temporal resolution in SVI over conventional voltage imaging, we applied a −100 to 50 mV voltage transient to HEK 293T cells expressing HVI-Cy3 and compared their fluorescence response using the two methods. The half-time ($t_{1/2}$) of HVI-Cy3 fluorescence response was calculated from the fluorescence traces measured in SVI (1474 Hz) or conventional voltage imaging (295 Hz) of the same regions of interest (ROIs) (Figure 2A). Our analysis reveals approximately 30% faster fluorescence response measured with SVI at 1474 Hz than measured at 295 Hz conventional voltage imaging (1.47 ± 0.09 ms versus 2.11 ± 0.07 ms, Figure 2B and C). The same trend was observed at a higher frame rate, with $t_{1/2}$ measured at 2343 Hz SVI 10.7% smaller than that measured at 471 Hz conventional method (1.59 ± 0.10 ms versus 1.79 ± 0.11 ms, Figures 2C and S6A). Notably, the response half-time monitored at 781 Hz SVI is almost half of that measured at 156 Hz conventional voltage imaging (1.49 ± 0.08 ms versus 3.35 ± 0.06 ms, Figure S6B−C). With ASAP3, our data also confirm that SVI provides approximately 30% higher temporal resolution than conventional imaging in reporting the V_m transient (3.80 ± 0.22 ms at 1474 Hz SVI versus 5.39 ± 0.33 ms at 295 Hz conventional voltage imaging, Figure S7).

The higher acquisition rate of SVI and faster response of GEVIs enable us to map the gap junction-mediated electrical coupling across a population of HEK 293T cells. Gap junctions are intercellular channels formed by connexin proteins,[25] which mediate the electrical coupling between neighboring cells that is essential for the synchronization of cardiac activities,[26] electrical synapses in neuronal signaling,[27] and

https://doi.org/10.1021/cbmi.3c00054
Chem. Biomed. Imaging 2023, 1, 448−460

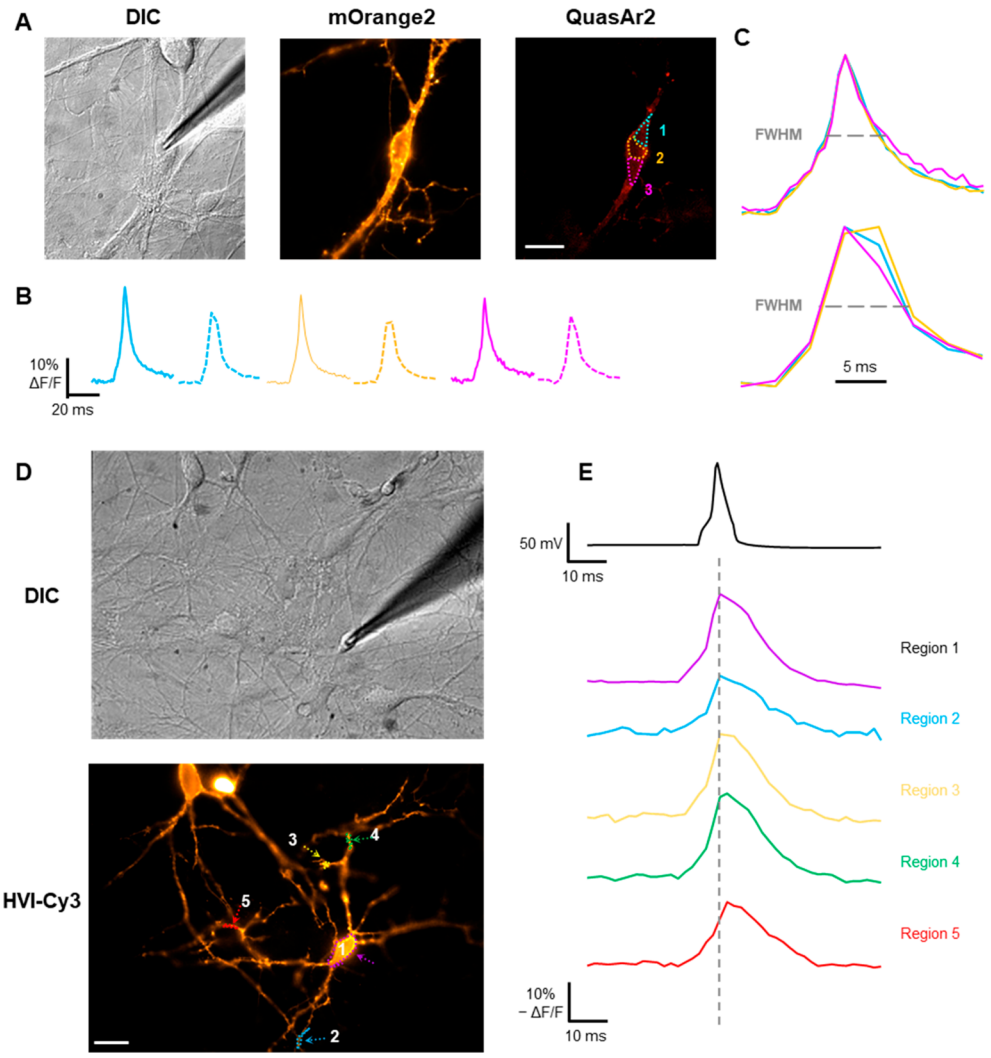

Figure 3. Stroboscopic voltage imaging realizes resolving action potential with better temporal resolution. (A) Brightfield and epifluorescence images of a rat hippocampal neuron expressing QuasAr2-mOrange2 with selected three somatic regions of interest (ROIs). (B) Corresponding optical traces of action potential (AP) evoked by current injection via SVI (solid lines, at 1474 Hz) and conventional method (dash lines, at 295 Hz) obtained from regions 1−3 in (A). The traces were generated from 150 AP repeats. (C) Zoom-in comparison of optical traces from SVI (top) and conventional method (bottom) in (B) aligned to the peak time of region 1. Gray dashed lines indicate the full-width at of the maxima of the traces. (D) Brightfield and epifluorescence images of rat hippocampal neurons expressing HVI-Cy3 with selected regions on the soma (region 1) and dendrites (regions 2−5). (E) Electrophysiological (top, black, acquired at 3932 Hz) and SVI signals from outlined regions in (D) (bottom, rainbow-colored, acquired at 983 Hz) of the evoked AP. The gray dashed line indicates the peak time in the optical trace of region 1. The electrical and optical traces were generated from 150 AP repeats. Scale bar = 20 μm.

pancreatic activity modulation.[28] We applied SVI to map the intercellular V_m depolarization propagation between HEK 293T cells expressing HVI-Cy3 within a 211 μm-by-112 μm FoV at 1474 Hz (Figure 2D). A −100 mV to 50 mV depolarization triggered by the patch clamp generated the depolarization wave from the clamped cell to neighboring cells. With data interpolation at 1000-fold upsampling,[9,29−31] a slow radial propagation (defined by the delay of $t_{1/2}$) from the clamped cell to the 11 neighboring cells could be visualized at micrometer spatial resolution.

At the higher acquisition rate of 1958 Hz SVI in an FoV of 93 μm-by-83 μm, we observed four adjacent cells responding rapidly with a delay shorter than 1 ms (Figure 2E and F), which indicated that the intercellular depolarization coupling was faster than 100 μm/ms. Additionally, a detailed mapping of the intracellular depolarization in five cells was visualized from pixel-level timing calculation after linear interpolation,[9] showing a location-dependent depolarization sequence from the location of the patch clamp pipet to the surrounding zone in the clamped cell, and from the proximal side to the triggered cell to the distal side in other four cells (Figure 2G). The above observations are consistent with the expected gap junction-mediated propagation of membrane potential. The accurate measurement of gap junction-mediated electrical coupling details in cell populations reveals that SVI is superior to conventional voltage imaging in resolving the bioelectrical events with a larger FoV and more precise timing readout.

To further illustrate the improved time accuracy of SVI, we compared the response time distribution of pixels from stroboscopic illumination and continuous illumination in a dye-based simulation to an AP-mimicking laser intensity fluctuation (Figure S8). We found that the response time to the globally synchronized fluorescence rise calculated from the continuous illumination data exhibited a location-dependent

https://doi.org/10.1021/cbmi.3c00054
Chem. Biomed. Imaging 2023, 1, 448−460

delay, assuming an opposite direction to the exposure delay in the rolling-shutter mode (Figure S8A). In contrast, the response time from the stroboscopic illumination data was much more synchronized, free of artifacts caused by the camera exposure delay (Figure S8B−D).

Implementation of SVI in Neurons

We next demonstrated SVI in recording neural activities with high fidelity and temporal resolution. We recorded AP in SVI via ASAP3, QuasAr2, and HVI and characterized the sensitivity and SNR in different compartments of neurons from 100 to 200 repeatable APs. The requirement of repeated data acquisition implies that SVI is vulnerable to photobleaching and phototoxicity. We thus compared the AP waveforms acquired by SVI with HVI-Cy3 across 300 APs over the time course of 1 min and found no statistically significant changes in either the sensitivity or the SNR (Figure S9).

When imaged with SVI at 1474 Hz, all GEVIs offered considerable sensitivities ($\Delta F/F_0$) to AP, while ASAP3 and QuasAr2 exhibited even slightly higher sensitivities versus the conventional voltage imaging at 295 Hz from the same cells (HVI-Cy3: −18.9% ± 0.8% versus −20.9% ± 1.2%; ASAP3: −20.2% ± 2.3% versus −19.3% ± 2.2%; QuasAr2:19.0% ± 1.5% versus 15.1% ± 0.7%, Figure S10A). The SNR of reporting AP in SVI was lower than that reported in the conventional method (HVI-Cy3:110.8 ± 12.3 versus 334.9 ± 55.6; ASAP3:56.9 ± 10.8 versus 60.3 ± 9.4; QuasAr2:115.2 ± 10.7 versus 119.1 ± 10.6, Figure S10B). By comparing the optical waveforms recorded in a cultured rat hippocampal neuron expressing QuasAr2 (Figure 3A), we confirmed that SVI enables the optical recording of AP with higher sensitivity and more details in AP shapes than conventional voltage imaging recorded in the same FoV (Figure 3B). Furthermore, SVI eliminated the rolling-shutter-induced severe distortion in the signals averaged from regions all on the soma but belonging to different lines on the camera, providing a more reasonable and uniform optical readout from the selected bordering areas (Figure 3C).

We then extended SVI to image back-propagating action potential (bpAP) on several dendrites in one rat hippocampus neuron. BpAPs propagate heterogeneously on the dendrites and take part in the localized depolarization on the distal ends, interacting with the excitatory postsynaptic potential (EPSP) or localized spikes evoked by dendritic activation and modulating the synaptic plasticity and information integration on the dendrites.[32,33] The speed and amplitude of bpAP propagating to the synaptic can involve spike-timing-dependent plasticity (STDP), introducing long-term potentiation (LTP) and long-term depression (LTD).[34,35] The bpAP dynamic on different types of neurons, separate dendrites of the identical neuron, or even on the various compartment on a single dendrite may be pretty different, affected by the differential expression of ion channels and heterogeneous in dendritic morphology.[36−40] Taking advantage of the much larger FoV in kHz SVI (Figure S11), we realized simultaneous measurement of bpAPs dynamic heterogeneity on distinct neurons without interpolation or fitting processing. When we stimulated the HVI-Cy3-expressing neuron to evoke somatic AP and performed SVI at 983 Hz in a 228 μm-by-166 μm FoV, we measured AP details on the soma and four dendritic regions with similar distances to the soma (Figure 3D and E). After aligning the electrical AP waveform from the soma and optical waveforms from the soma and ROIs on dendrites in time, we observed an apparent AP firing delay on the dendritic ROIs (2−5) to the soma (ROI 1), suggesting the occurrence of bpAP propagations. The discrepancy between peak location and signal details around the peak from dendritic ROIs implied different AP arrival times for the four ROIs early from ROI 2 to 5. In addition to the diversity in firing time, the amplitude of AP on ROI 2 and 5 exhibited apparent attenuation, while the ROI 3 and 4 originating from the same dendrite showed no recognizable attenuation. Across a 228 μm-by-166 μm FoV, SVI revealed the nonuniform bpAP propagation on distinct dendrites of one neuron without complex upsampling processing.

We leveraged the superior throughput and spatial resolution of optical recording to map the bpAP propagation details in a 211 μm-by-112 μm FoV at 1474 Hz SVI (Figure 4A and B). The AP timing delay images were calculated from the stimulated AP in a rat hippocampus neuron expressing HVI-Cy3, showing a nonuniform propagation of bpAP on the dendrites. Dendrites 2 and 3, with a larger diameter, featured a faster propagation with an over 250 μm/ms average velocity than dendrites 1 and 4 (Figure 4C). From the above, a higher acquisition rate and better timing accuracy in the larger FoV (i.e., rolling-shutter mode) enabled by SVI can boost the measurement of AP propagation details on the neurites.

All-Optical Electrophysiology with SVI

To map bpAP propagation on the dendrites in a larger FoV, we combined HVI-AF594 with a blue light-activated optogenetics tool, CheRiff, to achieve AP recording via all-optical electrophysiology in SVI (Figure 5A).[1] All-optical electrophysiology enables SVI to measure multiple FoV to follow bpAP propagation across a longer distance. To characterize the sensitivity and SNR of AP signals in different compartments of neurons (781 and 1474 Hz imaging with different FoVs), we evoked AP with 488 nm laser pulses and recorded the HVI-AF594 responses under SVI. HVI-AF594 could report the AP on the soma with decent sensitivity and SNR (at 781 Hz: −12.9% ± 0.7% with SNR of 107.1 ± 9.2; at 1474 Hz: −14.1% ± 0.5% with SNR of 82.4 ± 4.7, Figure S12A), with no significant differences to conventional voltage imaging conditions in sensitivity (at 156 Hz: −11.4% ± 0.6% with SNR of 193.7 ± 13.9; at 295 Hz: −14.1% ± 0.6% with SNR of 210.8 ± 26, respectively, Figure S12B). To confirm that the optical crosstalk in this platform is negligible, we recorded the optogenetics stimulation-related fluorescence fluctuation in the HVI-AF594-expressed neurons. We observed a stable crosstalk of 0.45% ± 0.21% $\Delta F/F_0$ under continuous illumination or a crosstalk of 1.48% ± 0.29% $\Delta F/F_0$ peak under SVI conditions, which is 1 order of magnitude lower than the sensitivity of HVI-AF594 to AP (Figure S13). To mitigate photobleaching and phototoxicity, we added 1.5 mM Trolox and 0.5 mM 1,3,5,7-cyclooctatetraene-1-carboxylic acid (COT-COOH), which were used as antioxidants in single-molecule imaging, into the imaging buffer.[41] We confirmed that these compounds did not interfere with the intrinsic excitability of the neurons (Figure S14).

To explore the bpAP propagation properties via SVI on a larger scale beyond the limit of the camera acquisition, we imaged the optogenetics-evoked AP in four subcellular sections, realizing a 460 μm-by-308 μm FoV (Figure 5B). The 781 Hz SVI imaging of the optogenetics-evoked AP was performed at the four locations in turn. bpAP propagation on the dendrites was calculated from the interpolated data image-

https://doi.org/10.1021/cbmi.3c00054
Chem. Biomed. Imaging 2023, 1, 448−460

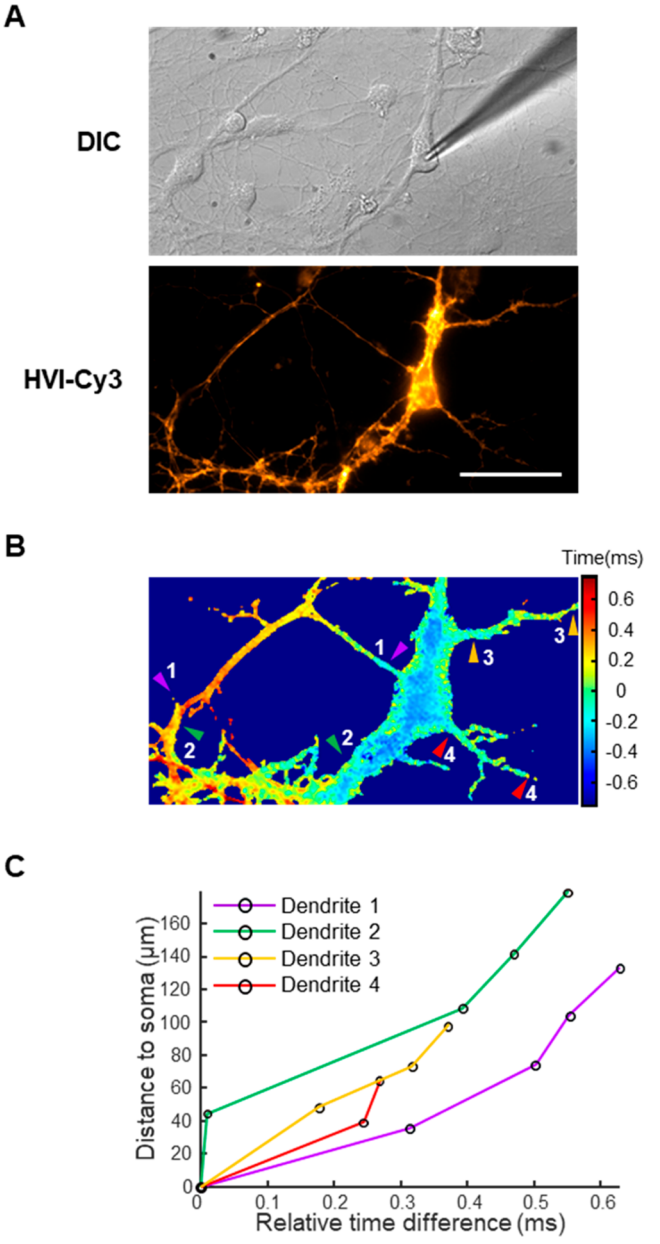

Figure 4. Stroboscopic voltage imaging measures long-range action potential propagation on the dendrites. (A) Brightfield and epifluorescence images of a rat hippocampal neuron expressing HVI-Cy3. (B) Map of AP propagation timing calculated for the field of view shown in (A) and extracted by the subframe linear interpolation to the 1474 Hz SVI (25 W/cm^2) movie generated from 200 somatic AP repeats evoked by current injection. The rainbow-colored arrows indicate four dendrites at different propagation speeds. (C) Difference distances to the soma plotted against the timing delay to the soma in dendrite 1−4 labeled in (B). Each point was calculated as the average time in a 1−8 μm^2 site on the dendrite.

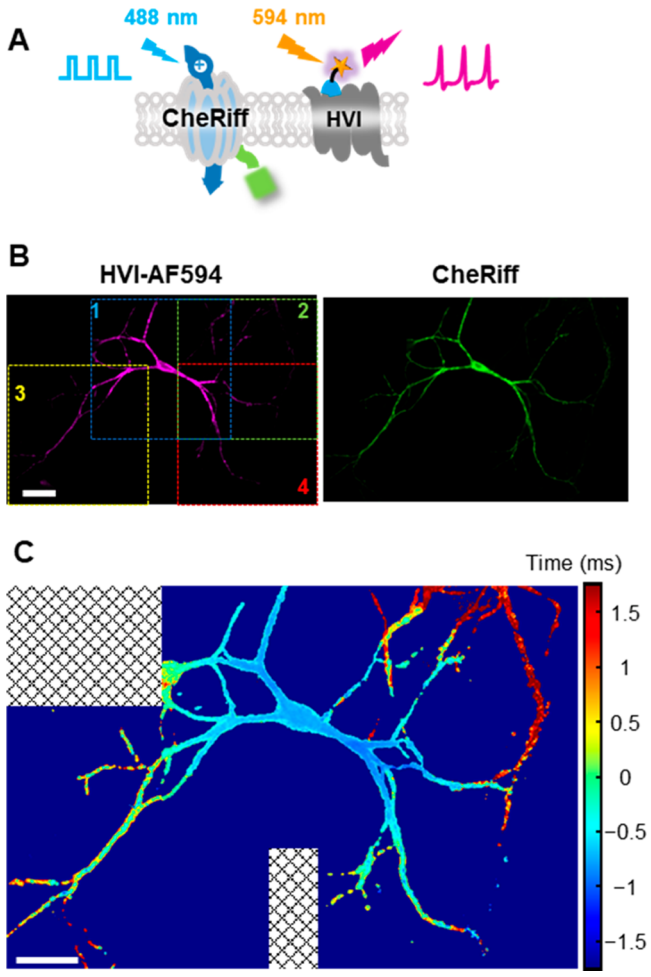

Figure 5. All-optical electrophysiology allows stroboscopic voltage imaging to measure large-scale action potential propagation. (A) Scheme of optical stimulation and recording of action potential in neurons coexpressing CheRiff-EGFP and HVI-AF594. (B) Reconstructed epifluorescence images of a rat hippocampal neuron expressing CheRiff-EGFP and HVI-AF594 with a 460 μm-by-308 μm field of view. The four dash squares represent the four image sections numbered in the order of all-optical electrophysiology-based SVI acquisition. For each section, 150 AP spikes were stimulated globally with 6.4 ms 2.0 mW/mm^2 488 nm laser pulse, and HVI-AF594 were simultaneously recorded under strobe 594 nm laser (11 W/cm^2) for generating SVI movies on the section. (C) Map of AP propagation timing collected from the results in four image sections shown in (B). The propagation timing was independently calculated in each image section from corresponding SVI movies extracted by subframe linear interpolation. After that, the results were merged by normalization of timing in the joint pixels of neighboring sections.

by-image. The global propagation map was reconstructed by combining the results in four sections aligned from the shared pixels in multiple subimages (Figure 5C). With the convenience of optical stimulation, we extended 781 Hz SVI to a submillimeter scale with an excellent spatial-temporal resolution to traditional voltage imaging and electrode-based techniques, promoting the research of AP dynamics on distal neurites. Compared to other large-scale voltage imaging applications, SVI is compatible with basic wide-field microscopic configurations and could realize neurite measurement via an objective with a higher magnification time and a larger numerical aperture, maintaining a decent SNR for resolving AP details.

DISCUSSION

Voltage imaging has several unique advantages in the throughput and spatial resolution over traditional electrode-based methods for mapping neural activities. However, the deficiency in temporal resolution and observation range, which is limited by the SNR of voltage indicators and the technology

https://doi.org/10.1021/cbmi.3c00054
Chem. Biomed. Imaging 2023, 1, 448−460

of cameras, restricts its application.[6] In contrast to the world of rapidly evolving GEVIs, there have been no major breakthroughs in the camera industry to offer high acquisition rates. sCMOS camera, benefiting from the rolling-shutter mode, provides larger FoV and less readout noise than the EMCCD camera but simultaneously introduces a nonsimultaneous exposure time, resulting in location-related signal distortion to voltage imaging on AP.

In this work, we develop a stroboscopic illumination-based voltage imaging method (SVI) in standard sCMOS camera configurations (i.e., rolling-shutter mode). Stroboscopic illumination technology has been applied to calcium imaging in sperm cells and voltage imaging in cardiomyocytes and hair cells in recording spontaneous events.[42−46] While stroboscopic illumination in these applications has successfully reduced the impact of phototoxicity and motion blur on imaging, it does not lead to an increase in the sampling rate. In contrast, our SVI scheme eliminates the rolling shutter-related artifacts and increases the acquisition rate by 5-fold as compared to the conventional methods.

In principle, this improvement in acquisition rate is also applicable to the global shutter mode of sCMOS cameras and EMCCD cameras. In terms of excitation configurations, as SVI requires modulating the duty cycle of the excitation light source and its phases relative to the camera exposure, it is necessary to maintain a submillisecond-level synchronization between the light source and the camera. Such synchronization could be readily achieved using a data acquisition board (such as National Instrument DAQ card). As long as synchronization is achieved, SVI could be compatible with alternative laser excitation configurations (e.g., confocal or light-sheet) or alternative light sources (e.g., stroboscopic xenon lamp or LED).[43,44,46]

Notably, an alternative method to achieve fast imaging in larger FoV is sequentially capturing the adjacent smaller FoVs and stitching them together under the conventional illumination scheme.[31] To improve the temporal resolution by 5-fold, the acquisition FoV is reduced by a factor of 5. While this imaging scheme is easier to implement by avoiding the application of stroboscopic illumination, it is not as photon budget-efficient at SVI. In each acquisition, the whole field is illuminated but only photons from the small FoVs are recorded by the camera, which causes a waste of the photon budget by as much as 80%. In contrast, the 5-phase SVI does not waste the photon budget, with the camera capturing photons from the larger FoV during each illumination.

Compared to interpolation-based upsampling algorithms (such as SNAPT) at the data analysis end to boost the timing accuracy of action potential wavefronts,[9,29−31] SVI acquires image series at a higher temporal resolution over a larger FoV on the data acquisition end, thus providing a better starting point for SNAPT-based analysis. It is also worth noting that a stand-alone upsampling algorithm cannot eliminate the signal distortion introduced by low sampling rates and rolling shutter-related artifacts of the raw data in each pixel. We therefore expect that SVI could be combined with SNAPT in future voltage imaging applications.

It is noteworthy that SVI requires repeated measurement of the same bioelectrical event, such as triggered firing of a single AP, and is thus incapable of recording spontaneous electrical activities. Parallel recording with a multicamera array has been applied to boost the FoV in high-speed biological imaging applications, such as the motion of organisms[47,48] and Ca^{2+} responses in cell ensembles.[49] Alternatively, the acquisition rate could be increased via temporal pixel multiplexing, which involves embedding several sequential image acquisition frames into a single camera exposure via a synchronized oscillatory projector.[50,51] These techniques offer attractive avenues to achieve kilohertz voltage imaging for capturing spontaneous events.

CONCLUSIONS

To summarize, we have developed a stroboscopic voltage imaging method that is fully compatible with commonly used GEVIs. In electrically coupled HEK 293T cells, SVI provides details of the depolarization initiation and propagation in a dozen of neighboring cells at 1958 Hz, allowing the tracking of fast depolarization wave (>100 μm/ms) across a 93 μm-by-83 μm FoV. Compared to conventional voltage imaging, SVI can prevent location-dependent distortion in reported voltage waveforms from bordering regions. We have demonstrated the power of SVI for monitoring the AP propagation on the neurites at kHz. SVI distinguishes the nonuniform speed and amplitude attenuation in distinct dendrites within the same neuron. With the combination of a high-sensitivity red GEVI HVI-AF594 to the optogenetics actuator CheRiff-EGFP, SVI enables multiple rounds of imaging for mapping the AP dynamics on the different dendrites in a 460 μm-by-308 μm FoV at 781 Hz, overcoming the limits to FoV from the camera. From this perspective, the novel red GEVIs with higher brightness, lower phototoxicity, and more orthogonal spectrum are welcomed as an opportunity to expand the FoV of SVI imaging.

METHODS

Cell Culture and Transfection

In the experiments described in Figures 1, 2, and S3−S7, human embryonic kidney 293T (HEK 293T) cells were maintained in Dulbecco's modified Eagle medium (DMEM, Gibco) supplemented with 10% fetal bovine serum (FBS, Gibco) and incubated at 37 °C in the presence of 5% CO_2. Prior to transfection, HEK 293T cells were seeded into a 24-well plate. At 70−90% confluency, cells were transfected with plasmids (500−750 ng/well) using Lipofectamine 2000 Reagent (Invitrogen) according to the manufacturer's instructions. After 24 h of transfection, cells were trypsinized and reseeded onto 12 mm glass coverslips (CellVis) precoated with matrigel matrix (Corning) to about 10% confluency for subsequent patch clamp electrophysiology and fluorescence imaging experiments (Figures 1C, 2B and C, and S3−S7), or to about 80% confluency for mapping the gap junction-mediated propagation (Figure 2D−G).

In the experiments of cultured rat hippocampus neurons related to Figures 3−5 and S9−S14, 12 mm glass coverslips were sterilized and coated with poly-D-lysine (10 μg/mL, Sigma-Aldrich) solution at 37 °C with 5% CO_2 for more than 24 h in a 24-well plate. The coverslips were rinsed twice with ddH_2O and incubated with Laminin Mouse Protein (10 μg/mL, Gibco) solution at 37 °C with 5% CO_2 overnight. Thereafter, the coverslips were washed twice with ddH_2O and air-dried at room temperature.

In the hippocampal neurons dissection, the heads of neonatal rats were separated from the bodies with scissors, and the brains were removed from the skull and placed into a 35 mm dish with a precooled dissection medium (High

https://doi.org/10.1021/cbmi.3c00054
Chem. Biomed. Imaging 2023, 1, 448−460

Glucose DMEM supplemented with penicillin/streptomycin antibiotics). The hippocampi were isolated from the brain under a dissection scope, cut into small pieces (approximately 0.1 mm^3), and digested with 2 mL Trypsin-EDTA (0.25%, Gibco) at 37 °C with 5% CO_2 for 15 min. The supernatant was removed gently and replaced with 1 mL DMEM containing 10% FBS. The tissue fragments were triturated via repeated pipetting for 1 min and incubated on an ice bath for 5 min. The supernatant was diluted by neuron culture medium (Neurobasal Medium, B-27 Supplement, GlutaMAX Supplement, and penicillin/streptomycin, all from Gibco) to a final cell density of 6×10^4 cells/mL. One mL cell suspension was added to each 24-well, and the medium was half-replaced with fresh medium once every 4 days.

Neurons were transfected on 8 days *in vitro* (DIV8) via lipid-mediated transfection. For each 24-well, 1000−1200 ng total plasmid DNA and 2−2.4 μL of Lipofectamine 3000 Reagent (Invitrogen) were separately diluted with Neurobasal Medium. Subsequently, the DNA solution was mixed with Lipofectamine 3000 Reagent and incubated with neurons for 40 to 60 min. Thereafter, the transfection reagent was replaced by the medium consisting of the original medium and fresh neuron culture medium (1:1 in volume). The transfected neurons are typically imaged at DIV11−15.

HVI Labeling of Cultured Hippocampal Neurons

The HVI-Cy3 and HVI-AF594 used in this work were based on the PRIME-IEDDA labeling, linking the fluorophores (Cy3-Tetrazine for HVI-Cy3 or AlexaFluor594-Tetrazine for HVI-AF594, all from Click Chemistry Tools) to the Ace2 rhodopsin mutant.[1,52] HEK 293T cells or neurons after transfection were incubated with a mixture of 5 μM engineered bacterial lipoic acid ligase mutant (^{W37V}LplA), 100 μM *rel*-(1*R*-4*E*-p*R*)-cyclooct-4-ene-1-yl-*N*-pentanoic acid carbamate (4-TCO), 1 mM ATP (Amresco), and 1 mM magnesium acetate (Sigma-Aldrich) in Tyrode's salt solution (Macgene Technology) for 30 min at 37 °C. The labeled cells were gently washed with Tyrode's buffer for 3 times and then labeled with 0.5 μM Cy3-Tetrazine or 0.8 μM AF594-Tetrazine in Tyrode's buffer for 10 min. Cells were washed another 3 times in the dark before the voltage imaging experiment.

Fluorescence Imaging Apparatus

All of the fluorescence imaging experiments were performed on an inverted fluorescence microscope (Nikon-TiE) equipped with a 40× 1.3 N.A. oil immersion objective lens, four laser lines (Coherent OBIS 488, 532, 594, and 637 nm) and a scientific CMOS camera (Hamamatsu ORCA-Flash 4.0 v2). The microscope, lasers, patch-clamp amplifier, and sCMOS camera were connected and synchronized with two data acquisition (DAQ) boards (PCI-6733 and PCIe-6353, National Instrument) and controlled via a customized software written in LabVIEW (National Instruments, version 15.0). In all experiments, the downsampling rate between DAQ I/O (patch-clamp and the laser for stroboscopic illumination and optogenetics stimulation) and the camera exposure was set to 20. The patch-clamp and laser output were triggered via the camera exposure in the recording, and the input patch-clamp data were low-pass filtered with an internal 5 kHz Bessel filter of the amplifier and digitized with the DAQ board at 20-time of the camera exposure rate.

The spectral properties of dichroic mirrors and emission filters for various fluorophores are summarized in Table S1. Fluorescence images and videos were acquired at 2-by-2 camera binning. Image analysis was performed in ImageJ/Fiji (NIH, version 1.53t) and MATLAB (Simulink, version 2018B).

Patch Clamp Electrophysiology

All live-cell imaging and patch-clamp electrophysiology experiments were performed at room temperature. The extracellular solution (XC) contains 125 mM NaCl, 2.5 mM KCl, 3 mM $CaCl_2$, 1 mM $MgCl_2$, 10 mM HEPES, and 30 mM glucose (all from Sigma-Aldrich) in the Tyrode's buffer. The pH of the XC was adjusted to 7.3 with 5 M NaOH (Sigma-Aldrich). The osmolarity of the XC was adjusted to 305−315 mOsm/kg with 1 M sucrose (Sigma-Aldrich) at room temperature. For patch-clamp experiments on HEK 293T cells (Figures 1C, 2B and C, and S3−S7), 50 μM 2-aminoethoxydiphenyl borate (2-APB, from Abcam) was added to the extracellular solution to inhibit the gap junction between HEK 293T cells. For imaging on the neurons expressing HVI-AF594 (Figures 5 and S12−S14), the XC contained 1.5 mM Trolox (Sigma-Aldrich) and 0.5 mM 1,3,5,7-cyclooctatetraene-1-carboxylic acid (COT-COOH, a gift from Prof. Zhixing Chen at Peking Univerisity).

The borosilicate glass electrodes (Sutter Instrument) were pulled to a tip resistance of 2.5−5 MΩ via a P-97 micropipette puller (Sutter Instrument) and filled with an internal solution (IC) containing 125 mM potassium gluconate, 8 mM NaCl, 0.6 mM $MgCl_2$, 0.1 mM $CaCl_2$, 1 mM EGTA, 10 mM HEPES (all from Sigma-Aldrich), 4 mM Mg-ATP, and 0.4 mM GTP-Na_2 (Shanghai Yuanye Bio-Technology). The pH of the IC was adjusted to 7.3 with 5 M KOH (Sigma-Aldrich). The osmolarity of the IC was adjusted to 290−300 mOsm/kg with 1 M sucrose.

In all patch-clamp experiments, glass electrodes were positioned by an MP-285 micromanipulator (Sutter Instrument), and the whole-cell recordings on HEK 293T cells and cultured neurons were performed with an Axopatch 200B amplifier (Axon Instruments). The membrane potential (V_m) of the clamped cells was held at −70 mV prior to subsequent simultaneous electrophysiological and optical recording, and the specific outputs for V_m manipulation (in voltage-clamp mode) or current injection (in current-clamp mode) were described in each experimental sections below. The input/output (I/O) signals for the patch-clamp amplifier were digitized with a data acquisition board (DAQ PCI-6733, National Instrument).

Impletion of Stroboscopic Illumination-Based Imaging

As described in Figures 1B and S1, SVI recording to repeatable electrical events requires five consecutive stroboscopic illumination series, each time shifting the phase of the pulsed illumination by 20% of the camera exposure time (starting from 0%, 20%, 40%, 60%, and 80% of one exposure with a 20% duty cycle). In addition, the onset of camera exposure is also shifted relative to the electrical signal (with −2/5, −1/5, 0, 1/5, and 2/5 phases of the exposure length). As the downsampling rate between the DAQ board (for illumination laser, optogenetics stimulation laser, and patch clamp output) and the camera was set to 20, the length of each stroboscopic illumination and shift in two adjacent exposure positions were equal to 4 data points in the DAQ command (Figure 1B). The clock frequency in the DAQ board and camera is different, so the 20-time downsampling rate between these two devices is impossible to be absolutely precise, inducing a "phase-shift" in stroboscopic illumination and camera exposure. We selected

https://doi.org/10.1021/cbmi.3c00054
Chem. Biomed. Imaging 2023, 1, 448−460

five pairs of camera exposure time and their corresponding DAQ board frequencies to mitigate the phase-shift-induced inaccuracy listed in Table S2. In these settings, the phase shift could be negligible in a 30-s-length acquisition for sensitivity characterization in Figures 1 and S3−S5, with the longest time in a single acquisition (i.e., 25 repeats of the electrical events) for complete SVI signals.

The rolling shutter mode of the sCMOS camera works in sequential exposure and readout in every horizontal line. Each line has the same exposure length and a linear delay in exposure timing from the centerlines to the borderlines in the FoV. The difference in exposure time results in fluorescence signal from specific stroboscopic illumination positions will be split into two consecutive exposure frames at most lines (Figure S1A). Due to the 20% duty cycle of each laser illumination to the exposure, in each horizontal line on the camera chip, only one of the five strobe light positions will be invalid. (Figure S1B).

The light pulse positions of five kinds of stroboscopic illumination starting at 0%, 20%, 40%, 60%, and 80% of the exposure length are named as 1, 2, 3, 4, and 5, respectively. The five exposure positions with −2/5, −1/5, 0, 1/5, and 2/5 phases (exposure length) different from the identical electrical event are named as A, B, C, D, and E (Figure S1C). The five light pulse positions and five exposure positions can be pairwise combined into 25 imaging conditions, and the imaging of a repeatable electrical event (e.g., current injection-evoked AP spikes) is performed in order of A1−5, B1−5, C1−5, D1−5, and E1−5 (Figure S1C). After the time correction and averaging, the SVI movie of a repeatable electrical event can be reconstructed from these 25 imaging units (Figures S1D and S2).

The time in the 25 imaging units with different camera exposure positions should be aligned to the camera exposure position "A" described before and shown in Figure S1C. Figure S2A is an example of the data averaged from the pixel in horizontal line 55 (from top to bottom) in 1474 Hz SVI FoV whose total line number is 688. Thus, line 55 is located at the "0%−10%" region described in Figure S1A and B. In the time alignment of the data with exposure positions B, C, D, and E, their time axis should be translated by 1, 2, 3, and 4 SVI frames (i.e., 1/5, 2/5, 3/5, and 4/5 camera exposure length, or 4, 8, 12, and 16 DAQ data points) to the left (Figure S2A). The simple translation of the data from various exposure positions provides data from five acquisition times on each SVI data point with a five-time acquisition rate as the conventional method. However, it does not eliminate the fluorescence split-related intensity bias in the 1/5 SVI data on every frame. In the SVI frames, the results of $\text{Number}_{\text{frame}}$ modulo 5 indicate the original positions of the stroboscopic illumination ($\text{Number}_{\text{frame}} \equiv 0$, 1, 2, 3, or 4 (mod 5) means the stroboscopic illumination position is 5,1,2,3, or 4), determining the camera exposure position providing invalid data in the SVI frame at the pixel. The correspondence between the exposure delay-induced invalid data on each location in FoV (horizontal line number) and the stroboscopic illumination or camera exposure position in the aligned SVI data is listed in Figure S2B. As an example shown in Figure S2C, a zoom-in display of the frames around the peak (Frame 47) in the "after time alignment" plot in Figure S2A, labels in teal blue highlight the attribution of the camera exposure position (A-E) to the 1/5 outlier data. The final SVI data in each frame will be averaged from the 4 of the 5 camera exposure positions' data without being contaminated by the rolling shutter-related exposure delay, realizing a 5-time acquisition rate with better time accuracy than the conventional voltage imaging in the same FoV (Figures 1B and S2D).

Linear Interpolation of Subframe Timing

For mapping the intracellular and intercellular V_m depolarization propagation at the pixel level (Figures 2D and G, 4B, and 5C), linear interpolation was introduced to the normalized SVI trace of the electrical events on each pixel. The method is adapted from the subframe interpolation approach to analyzing AP propagation from voltage imaging data.[9,29−31,40] The SVI data of fluorescence fluctuation will first be denoised with a Gaussian spatial filter and principal components analysis (PCA)-based temporal filter. After excluding the pixel with a lower standard deviation in the frames, the linear interpolation will be performed on the rest pixel-of-interest, achieving 1000-time upsampling. On each pixel, the time that the fluorescence trace first passes over the customized threshold (50% of maximum fluorescence change in this work) will be defined as the arrival time of the electrical events, and the sum of the calculated time on pixels will be normalized to zero for the final propagation heat maps. The propagation movie from the subframe linear interpolation results was generated by a Gaussian time distribution with a Δt = 0.025 ms and global-average temporal resolution σ = 0.025 ms[9]. The brightness time of each pixel was equal to the arrival timing calculated above. The image sequences (Δt = 0.1 ms) were selected from the movie and displayed sequentially (Figure 2G).

Simulated Stroboscopic Imaging of Fluorescein Solution

A 500 nM fluorescein solution was used to provide an extremely high $\Delta F/F_0$ for validating the temporal accuracy and system bias in SVI (Figures S2 and S8). An action potential-mimicking (with an fwhm of 10 ms and a 900% $\Delta F/F_0$ between the intensity on the peak and the "resting" baseline) output signal was applied to the 488 nm laser under stroboscopic or continuous illumination to generate the GEVI response-like fluorescence fluctuation on the pixels in SVI mode (Figures S2A and S8B) or conventional voltage imaging mode (Figure S8A), with about 750% $\Delta F/F_0$ fluorescence change. For examination of the synchronization to the fluorescence change induced by the laser intensity change, the time that the fluorescence trace first passes over the 50% of maximum fluorescence change was defined as the arrival time of the electrical events on each pixel in FoV (Figure S8A and B). The average time in each horizontal and vertical line was plotted against the line number (from top to bottom or left to right) for further comparison (Figure S8C and D).

Simultaneous Voltage Clamp and Optical Recording in HEK 293T Cells

For sensitivity ($\Delta F/F_0$) characterization of GEVIs in SVI and conventional voltage imaging (Figures 1C, 2B and C, and S3−S7), the V_m of HEK 293T cells was controlled via whole-cell voltage-clamp at a holding voltage of −70 mV and was stepped from −70 to −100, −40, −20, 0, 30, and 50 mV. Each V_m step lasted about 64 ms, and fluorescence changes were normalized to the baseline fluorescence at V_m = −70 mV. Data were acquired at 1474 and 295 Hz for stroboscopic and conventional voltage imaging, respectively. The single acquisition consisting of 25-times stimulation is about 30.5 s. The final traces were reconstructed from twice acquisitions for SVI data,

https://doi.org/10.1021/cbmi.3c00054
Chem. Biomed. Imaging 2023, 1, 448−460

and the conventional voltage imaging data were generated from a single acquisition.

For kinetic characterization of GEVIs in SVI and conventional voltage imaging, a V_m pulse-like transient from −100 mV to 50 mV was applied to the cell, and the V_m depolarization lasted about 239 ms. The single acquisition consisting of 25-time depolarization/repolarization is about 14.6 s. The final traces were averaged from three times of acquisitions for 2343, 1474, and 781 Hz SVI and the corresponding 471, 295, and 156 Hz conventional voltage imaging data. The response kinetics in two imaging settings were evaluated at the duration from the depolarization to the time when the fluorescence trace of the cells crossed 50% of maximum fluorescence change ($t_{1/2}$).

Mapping Gap Junction-Mediated Electrical Coupling in HEK 293T Cells

For monitoring depolarization propagation (Figure 2D−G) in the cell population, a whole-cell voltage clamp was established in a cell surrounded by high-density cells expressing the GEVI (HVI-Cy3 or Ace-D81S-mOrange2). The depolarization propagation was triggered by a −100 to 50 mV V_m transient to the clamped cell, and the depolarization would be measured in the clamped cell and surrounding cells with 1474 (Figure 2D) and 1958 Hz (Figure 2E−G) SVI. The single acquisition consisting of 25-time depolarization is about 14.6 s, and the final SVI data were averaged from two or four times of acquisitions. The time that the fluorescence trace from selected cell regions (Figure 2Eand F) or on each pixel (Figure 2D and G) first passes over the customized threshold (50% of maximum fluorescence change in this work) will be defined as the arrival time of the electrical events, and the velocity between each selected region was calculated by dividing the distance between two cells by the time delay.

Simultaneous Current Clamp and Optical Recording in Cultured Neurons

For characterizing the sensitivity and waveform accuracy of detecting AP in SVI and conventional voltage imaging method in the cultured rat hippocampal neurons (Figures 3 and S9−10), a whole-cell current injection (120−300 pA, 8 ms) and simultaneous imaging were established in the neuron expressing the HVI-Cy3, QuasAr2, and ASAP3 and evoked the 4−5 Hz spike trains. The single acquisition consisting of 25 AP of SVI is about 5.5−6.4 ms, and the final SVI data were reconstructed from 100 to 200 APs at 1474 Hz, while the AP traces of comparative conventional voltage imaging methods was averaged from 50 APs at 295 Hz.

All-Optical Electrophysiology with SVI in Cultured Neurons

Cultured rat hippocampal neurons coexpressing CheRiff-EGFP and HVI-AF594 were optogenetically stimulated with a 6.4−8 ms 488 nm Laser pulse (2 mW/mm^2) for a 5 Hz spike trains, and the single acquisition consisting of 25 AP of SVI is about 5.5 ms. For the characterization of the sensitivity and signal-to-noise ratio (SNR) of HVI-AF594 on reporting AP in SVI and conventional voltage imaging method, 100−200 APs were used to reconstruct the SVI data, and the conventional data were averaged from the fluorescence fluctuation of 50 APs. The SNR was calculated as the ratio of maximum fluorescence change over the root mean squared error (RMSE) of the linear-fitted trend line from 60 ms data of baseline fluorescence fluctuations. The sensitivity and SNR were collected at 1474 Hz/781 Hz in SVI and 295 Hz/156 Hz in the conventional method.

The AP arrival timing in each subregion was calculated independently to map the large-scale AP propagation details from multiple rounds of all-optical electrophysiology experiments in SVI. And AP propagation delay heatmaps were stitched together by normalization on the time of the shared pixels in neighboring subregions (Figure 5C).

To evaluate the crosstalk between the HVI-AF594 imaging channel and the 488 nm stimulation channel, the same all-optical electrophysiology experimental workflow was performed on the fixed neurons coexpressing CheRiff-EGFP and HVI-AF594, which eliminated the V_m-dependent response of AF594 dye to the stimulation on CheRiff. The crosstalk was evaluated as the maximum $\Delta F/F_0$ in 781 Hz SVI conditions (11 W/cm^2 594 nm laser excitation with a 20% duty cycle and a 6.4 ms 2 mW/mm^2 488 nm light pulse, Figure S13A, calculated from 200 times of 488 nm light pulse), and the stable crosstalk $\Delta F/F_0$ in 156 Hz continuous illumination imaging mode (2.2 W/cm^2 594 nm laser excitation and a 2 mW/mm^2 488 constant illumination, Figure S13B, calculated from 5 times of continuous 488 nm illumination).

■ ASSOCIATED CONTENT

Supporting Information

The Supporting Information is available free of charge at https://pubs.acs.org/doi/10.1021/cbmi.3c00054.

Detailed description and examination of implementing SVI on the sCMOS camera, the introduction of imaging apparatus, sensitivity and SNR characterization of various GEVIs on SVI, and the optical crosstalk and cell compatibility characterization of all-optical electrophysiology via CheRiff and HVI-AF594 (PDF)

■ AUTHOR INFORMATION

Corresponding Author

Peng Zou − *College of Chemistry and Molecular Engineering, Synthetic and Functional Biomolecules Center, Beijing National Laboratory for Molecular Sciences, Key Laboratory of Bioorganic Chemistry and Molecular Engineering of Ministry of Education, Peking University, Beijing 100871, China; PKU-IDG/McGovern Institute for Brain Research, Peking University, Beijing 100871, China; Chinese Institute for Brain Research (CIBR), Beijing 102206, China;* orcid.org/0000-0002-9798-5242; Email: zoupeng@pku.edu.cn

Author

Luxin Peng − *College of Chemistry and Molecular Engineering, Synthetic and Functional Biomolecules Center, Beijing National Laboratory for Molecular Sciences, Key Laboratory of Bioorganic Chemistry and Molecular Engineering of Ministry of Education, Peking University, Beijing 100871, China*

Complete contact information is available at: https://pubs.acs.org/10.1021/cbmi.3c00054

Author Contributions

P.Z. conceived the project. L.P. and P.Z. designed experiments. L.P. performed all experiments. L.P. and P.Z. analyzed data and wrote the paper.

https://doi.org/10.1021/cbmi.3c00054
Chem. Biomed. Imaging 2023, 1, 448−460

Notes

The authors declare no competing financial interest.

■ ACKNOWLEDGMENTS

We thank all lab members for helpful discussions. We thank Prof. Zhixing Chen (Peking University) for providing 1,3,5,7-cyclooctatetraene-1-carboxylic acid (COT-COOH). This work was supported by the Ministry of Science and Technology (2022YFA1304700, 2018YFA0507600), the National Natural Science Foundation of China (32088101). P.Z. is sponsored by Bayer Investigator Award.

■ REFERENCES

(1) Liu, S.; Lin, C.; Xu, Y.; Luo, H.; Peng, L.; Zeng, X.; et al. A far-red hybrid voltage indicator enabled by bioorthogonal engineering of rhodopsin on live neurons. *Nat. Chem.* **2021**, *13* (5), 472−479.
(2) Han, Y.; Yang, J.; Li, Y.; Chen, Y.; Ren, H.; Ding, R. et al. Bright and sensitive red voltage indicators for imaging action potentials in brain slices and pancreatic islets. *bioRxiv*, December 1, 2022, ver. 1. DOI: 10.1101/2022.12.01.518652.
(3) Fan, L. Z.; Kim, D. K.; Jennings, J. H.; Tian, H.; Wang, P. Y.; Ramakrishnan, C.; et al. All-optical physiology resolves a synaptic basis for behavioral timescale plasticity. *Cell* **2023**, *186* (3), 543−559.
(4) Abdelfattah, A. S.; Kawashima, T.; Singh, A.; Novak, O.; Liu, H.; Shuai, Y.; et al. Bright and photostable chemigenetic indicators for extended *in vivo* voltage imaging. *Science* **2019**, *365* (6454), 699−704.
(5) Liu, Z.; Lu, X.; Villette, V.; Gou, Y.; Colbert, K. L.; Lai, S.; et al. Sustained deep-tissue voltage recording using a fast indicator evolved for two-photon microscopy. *Cell* **2022**, *185* (18), 3408−3425.
(6) Emmenegger, V.; Obien, M. E. J.; Franke, F.; Hierlemann, A. Technologies to study action potential propagation with a focus on HD-MEAs. *Front. Cell. Neurosci.* **2019**, *13*, 159.
(7) Xu, Y.; Zou, P.; Cohen, A. E. Voltage imaging with genetically encoded indicators. *Curr. Opin. Chem. Biol.* **2017**, *39*, 1−10.
(8) Villette, V.; Chavarha, M.; Dimov, I. K.; Bradley, J.; Pradhan, L.; Mathieu, B.; et al. Ultrafast two-photon imaging of a high-gain voltage indicator in awake behaving mice. *Cell* **2019**, *179* (7), 1590−1608.
(9) Hochbaum, D. R.; Zhao, Y.; Farhi, S. L.; Klapoetke, N.; Werley, C. A.; Kapoor, V.; et al. All-optical electrophysiology in mammalian neurons using engineered microbial rhodopsins. *Nat. Methods* **2014**, *11*, 825−833.
(10) Liu, S.; Yang, J.; Zou, P. Bringing together the best of chemistry and biology: hybrid indicators for imaging neuronal membrane potential. *J. Neurosci. Methods* **2021**, *363*, 109348.
(11) Bando, Y.; Grimm, C.; Cornejo, V. H.; Yuste, R. Genetic voltage indicators. *BMC Biol.* **2019**, *17* (1), 71.
(12) Knöpfel, T.; Song, C. Optical voltage imaging in neurons: moving from technology development to practical tool. *Nat. Rev. Neurosci.* **2019**, *20* (12), 719−727.
(13) Chen, X.; Zeng, Z.; Li, R.; Xue, B.; Xi, P.; Sun, Y. Superior performance with sCMOS over EMCCD in super-resolution optical fluctuation imaging. *J. Biomed. Opt.* **2016**, *21* (6), 066007.
(14) Baker, M. Faster frames, clearer pictures. *Nat. Methods* **2011**, *8* (12), 1005−1009.
(15) Cutting, J. E. Representing motion in a static image: constraints and parallels in art, science, and popular culture. *Perception* **2002**, *31* (10), 1165−1193.
(16) Bartlett, R. *Introduction to sports biomechanics: Analysing human movement patterns*; Routledge: 2014.
(17) Elf, J.; Li, G.-W.; Xie, X. S. Probing transcription factor dynamics at the single-molecule level in a living cell. *Science* **2007**, *316* (5828), 1191−1194.
(18) Xiang, L.; Chen, K.; Yan, R.; Li, W.; Xu, K. Single-molecule displacement mapping unveils nanoscale heterogeneities in intracellular diffusivity. *Nat. Methods* **2020**, *17* (5), 524−530.
(19) Choi, A. A.; Xiang, L.; Li, W.; Xu, K. Single-molecule displacement mapping indicates unhindered intracellular diffusion of small ($\lesssim$1 kDa) solutes. *J. Am. Chem. Soc.* **2023**, *145*, 8510.
(20) Nicholson, D. A.; Nesbitt, D. J. Pushing camera-based single-molecule kinetic measurements to the frame acquisition limit with stroboscopic smFRET. *J. Phys. Chem. B* **2021**, *125* (23), 6080−6089.
(21) Chen, T.-Y.; Santiago, A. G.; Jung, W.; Krzemiński, L.; Yang, F.; Martell, D. J.; et al. Concentration- and chromosome-organization-dependent regulator unbinding from DNA for transcription regulation in living cells. *Nat. Commun.* **2015**, *6* (1), 7445.
(22) Brinks, D.; Klein, A. J.; Cohen, A. E. Two-photon lifetime imaging of voltage indicating proteins as a probe of absolute membrane voltage. *Biophys. J.* **2015**, *109* (5), 914−921.
(23) Chien, M.-P.; Brinks, D.; Testa-Silva, G.; Tian, H.; Phil Brooks, F.; Adam, Y.; et al. Photoactivated voltage imaging in tissue with an archaerhodopsin-derived reporter. *Sci. Adv.* **2021**, *7* (19), No. eabe3216.
(24) Xu, Y.; Deng, M.; Zhang, S.; Yang, J.; Peng, L.; Chu, J.; et al. Imaging neuronal activity with fast and sensitive red-shifted electrochromic FRET indicators. *ACS Chem. Neurosci.* **2019**, *10* (12), 4768−4775.
(25) Kumar, N. M.; Gilula, N. B. The gap junction communication channel. *Cell* **1996**, *84* (3), 381−388.
(26) Dhein, S. Gap junction channels in the cardiovascular system: pharmacological and physiological modulation. *Trends Pharmacol. Sci.* **1998**, *19* (6), 229−241.
(27) Rozental, R.; Giaume, C.; Spray, D. C. Gap junctions in the nervous system. *Brain Res. Rev.* **2000**, *32* (1), 11−15.
(28) Benninger, R. K.; Zhang, M.; Head, W. S.; Satin, L. S.; Piston, D. W. Gap junction coupling and calcium waves in the pancreatic islet. *Biophys. J.* **2008**, *95* (11), 5048−5061.
(29) Foust, A.; Popovic, M.; Zecevic, D.; McCormick, D. A. Action potentials initiate in the axon initial segment and propagate through axon collaterals reliably in cerebellar Purkinje neurons. *J. Neurosci.* **2010**, *30* (20), 6891−6902.
(30) Popovic, M. A.; Foust, A. J.; McCormick, D. A.; Zecevic, D. The spatio-temporal characteristics of action potential initiation in layer 5 pyramidal neurons: a voltage imaging study. *J. Physiol.* **2011**, *589* (17), 4167−4187.
(31) Gonzalez Sabater, V.; Rigby, M.; Burrone, J. Voltage-gated potassium channels ensure action potential shape fidelity in distal axons. *J. Neurosci.* **2021**, *41* (25), 5372−5385.
(32) Stuart, G. J.; Häusser, M. Dendritic coincidence detection of EPSPs and action potentials. *Nat. Neurosci.* **2001**, *4* (1), 63−71.
(33) Waters, J.; Helmchen, F. Boosting of action potential backpropagation by neocortical network activity *in vivo*. *J. Neurosci.* **2004**, *24* (49), 11127−11136.
(34) Linden, D. J. The return of the spike: postsynaptic action potentials and the induction of LTP and LTD. *Neuron* **1999**, *22* (4), 661−666.
(35) Caporale, N.; Dan, Y. Spike timing-dependent plasticity: a Hebbian learning rule. *Annu. Rev. Neurosci.* **2008**, *31*, 25−46.
(36) Häusser, M.; Spruston, N.; Stuart, G. J. Diversity and dynamics of dendritic signaling. *Science* **2000**, *290* (5492), 739−744.
(37) Vetter, P.; Roth, A.; Häusser, M. Propagation of action potentials in dendrites depends on dendritic morphology. *J. Neurophysiol.* **2001**, *85* (2), 926−937.
(38) Hoffman, D. A.; Magee, J. C.; Colbert, C. M.; Johnston, D. K^+ channel regulation of signal propagation in dendrites of hippocampal pyramidal neurons. *Nature* **1997**, *387* (6636), 869−875.
(39) Nevian, T.; Larkum, M. E.; Polsky, A.; Schiller, J. Properties of basal dendrites of layer 5 pyramidal neurons: a direct patch-clamp recording study. *Nat. Neurosci.* **2007**, *10* (2), 206−214.
(40) Tian, W.; Peng, L.; Zhao, M.; Tao, L.; Zou, P.; Zhang, Y. Dendritic morphology affects the velocity and amplitude of back-propagating action potentials. *Neurosci. Bull.* **2022**, *38* (11), 1330−1346.

(41) Altman, R. B.; Terry, D. S.; Zhou, Z.; Zheng, Q.; Geggier, P.; Kolster, R. A.; et al. Cyanine fluorophore derivatives with enhanced photostability. *Nat. Methods* **2012**, *9* (1), 68−71.
(42) Nishigaki, T.; Wood, C. D.; Shiba, K.; Baba, S. A.; Darszon, A. Stroboscopic illumination using light-emitting diodes reduces phototoxicity in fluorescence cell imaging. *Biotechniques* **2006**, *41* (2), 191−197.
(43) Entcheva, E.; Kostov, Y.; Tchernev, E.; Tung, L. Fluorescence imaging of electrical activity in cardiac cells using an all-solid-state system. *IEEE. Trans. Biomed. Eng.* **2004**, *51* (2), 333−341.
(44) Bachtel, A. D.; Gray, R. A.; Stohlman, J. M.; Bourgeois, E. B.; Pollard, A. E.; Rogers, J. M. A novel approach to dual excitation ratiometric optical mapping of cardiac action potentials with Di-4-ANEPPS using pulsed LED excitation. *IEEE. Trans. Biomed. Eng.* **2011**, *58* (7), 2120−2126.
(45) Fisher, J. A.; Kowalik, L.; Hudspeth, A. Imaging electrical resonance in hair cells. *Proc. Natl. Acad. Sci. U.S.A.* **2011**, *108* (4), 1651−1656.
(46) Suarez, S. S.; Varosi, S. M.; Dai, X. Intracellular calcium increases with hyperactivation in intact, moving hamster sperm and oscillates with the flagellar beat cycle. *Proc. Natl. Acad. Sci. U.S.A.* **1993**, *90* (10), 4660−4664.
(47) Thomson, E. E.; Harfouche, M.; Kim, K.; Konda, P. C.; Seitz, C. W.; Cooke, C.; et al. Gigapixel imaging with a novel multi-camera array microscope. *eLife* **2022**, *11*, No. e74988.
(48) Zhou, K. C.; Harfouche, M.; Cooke, C. L.; Park, J.; Konda, P. C.; Kreiss, L.; et al. Parallelized computational 3D video microscopy of freely moving organisms at multiple gigapixels per second. *Nat. Photonics* **2023**, *17*, 442−450.
(49) Fan, J.; Suo, J.; Wu, J.; Xie, H.; Shen, Y.; Chen, F.; et al. Video-rate imaging of biological dynamics at centimetre scale and micrometre resolution. *Nat. Photonics* **2019**, *13* (11), 809−816.
(50) Bub, G.; Tecza, M.; Helmes, M.; Lee, P.; Kohl, P. Temporal pixel multiplexing for simultaneous high-speed, high-resolution imaging. *Nat. Methods* **2010**, *7* (3), 209−211.
(51) Liang, J.; Wang, P.; Zhu, L.; Wang, L. V. Single-shot stereo-polarimetric compressed ultrafast photography for light-speed observation of high-dimensional optical transients with picosecond resolution. *Nat. Commun.* **2020**, *11* (1), 5252.
(52) Liu, D. S.; Tangpeerachaikul, A.; Selvaraj, R.; Taylor, M. T.; Fox, J. M.; Ting, A. Y. Diels-Alder cycloaddition for fluorophore targeting to specific proteins inside living cells. *J. Am. Chem. Soc.* **2012**, *134* (2), 792−795.

https://doi.org/10.1021/cbmi.3c00054
Chem. Biomed. Imaging 2023, 1, 448−460